

# Learning-based estimation of dielectric properties and tissue density in head models for personalized radio-frequency dosimetry

Essam A Rashed<sup>1,2,3</sup>, Yinliang Diao<sup>1,4</sup>, Akimasa Hirata<sup>1,5</sup>

<sup>1</sup>Department of Electrical and Mechanical Engineering, Nagoya Institute of Technology, Nagoya 466-8555, Japan

<sup>2</sup>Department of Computer Science, Faculty of Informatics & Computer Science, The British University in Egypt, Cairo 11837, Egypt

<sup>3</sup>Department of Mathematics, Faculty of Science, Suez Canal University, Ismailia 41522, Egypt

<sup>4</sup>College of Electronic Engineering, South China Agricultural University, Guangzhou 510642, China

<sup>5</sup>Center of Biomedical Physics and Information Technology, Nagoya Institute of Technology, Nagoya 466-8555, Japan

E-mail: [essam.rashed@nitech.ac.jp](mailto:essam.rashed@nitech.ac.jp)

**Abstract.** Radio-frequency dosimetry is an important process in human safety and for compliance of related products. Recently, computational human models generated from medical images have often been used for such assessment, especially to consider the inter-variability of subjects. However, the common procedure to develop personalized models is time consuming because it involves excessive segmentation of several components that represent different biological tissues, which limits the inter-variability assessment of radiation safety based on personalized dosimetry. Deep learning methods have been shown to be a powerful approach for pattern recognition and signal analysis. Convolutional neural networks with deep architecture are proven robust for feature extraction and image mapping in several biomedical applications. In this study, we develop a learning-based approach for fast and accurate estimation of the dielectric properties and density of tissues directly from magnetic resonance images in a single shot. The smooth distribution of the dielectric properties in head models, which is realized using a process without tissue segmentation, improves the smoothness of the specific absorption rate (SAR) distribution compared with that in the commonly used procedure. The estimated SAR distributions, as well as that averaged over 10-g of tissue in a cubic shape, are found to be highly consistent with those computed using the conventional methods that employ segmentation.

Keywords: Electromagnetic exposure, radio frequency, human safety, deep learning, specific absorption rate (SAR)

## 1. Introduction

In the last few decades, many anatomical human models have been developed, especially for computational dosimetry (Nagaoka et al. 2004, Dimbylow 1997, Christ et al. 2005, Lee et al. 2015), to quantify the induced physical quantities in a target tissue for electromagnetic-field exposure. Such models have been developed from different types of medical images, e.g., magnetic resonance imaging (MRI), computed tomography (CT), and other modalities. Typically, the models are segmented into several tissue types for the head and approximately 50 or more for the whole body. In general, identical physical constants are assigned to each tissue. For example, in human-head studies, the standard process is to segment all (or the major) head tissues and then use tissue-based measurements from the literature to identify the physical properties of the segmented model.

The disadvantage of this conventional approach is that a single set of physical constants is uniformly assigned to each annotated tissue. This assumption is unrealistic because even within the same tissue, the dielectric properties can vary based on different parameters such as water content (Michel et al. 2017), sodium concentration (Liao et al. 2019), and anatomical structure. This biological phenomenon is notable especially in the tissue border regions where the tissue physical properties have large differences (Gurler & Ider 2017). Moreover, segmentation is usually conducted using different approaches, which may lead to high variability in dosimetry studies. Accurate segmentation is usually considered as a computationally expensive process that limits its feasibility for clinical use.

To avoid potential errors caused by segmentation faults, several methods have been proposed to directly estimate the tissue electrical/dielectric properties based on anatomical images (e.g. Ropella & Noll 2017, Elsaid et al. 2017, Hampe et al. 2019, Serralles et al. 2019). The water content calculated from T1-weighted MRI scans is modeled using a monotonic function to estimate the conductivity of major brain tissues (Tuch et al. 2001). However, such methods utilize data that are strictly limited to the brain only. Magnetic resonance electrical impedance tomography (MREIT) has been proposed as a useful approach to estimate brain conductivity (Chauhan et al. 2018, Kwon et al. 2016, Kwon et al. 2014). However, it is also strictly limited to brain tissues. A recent review of the methods used to estimate the electrical conductivity based on MRI scans was presented in (Liu et al. 2017). In addition to the electrical conductivity, relative permittivity is required in radio-frequency dosimetry. Moreover, tissue density is required for the specific absorption rate (SAR) computations.

Learning-based techniques are now the state of the art in several pattern-recognition and data-labeling problems (Bengio et al. 2013). Interesting achievements can be observed, and significant improvement has been reported in the past few years compared with the conventional methods. The most important key for the success of the learning-based approaches is the architecture depth that enables better extraction of important features without the need for prior engineering or customized regularizers. In particular,

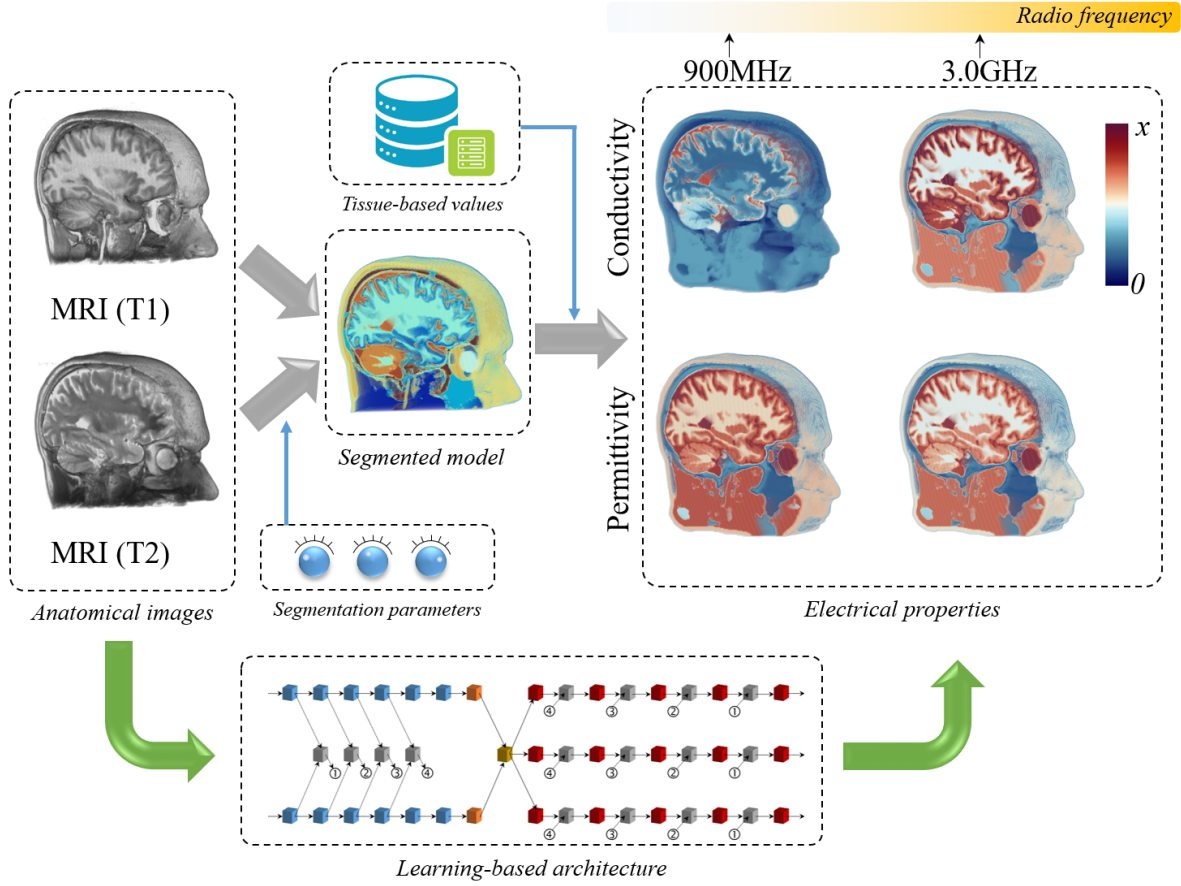


**Figure 1.** The current standard pipeline for the uniform conductivity ( $\sigma$ ) and relative permittivity ( $\epsilon$ ) map computations is shown by gray arrows. The anatomical images are segmented to generate the annotated head model. Then, the tissue-based electrical properties are assigned to each tissue based on the desired frequency. Finally, different conductivity and relative permittivity models are generated using the tissue-based uniform values. The green arrows indicate the contribution of this study in which several parameter adjustments can be avoided using the learning-based architecture. The values are  $x = 3.0$  S/m and  $x = 70$  in the conductivity and permittivity maps, respectively.

convolutional neural networks (CNNs) are now the leading tool for image processing and recognition.

For human exposure to non-ionizing electromagnetic fields below the frequency of 300 GHz, two regimes exist from the viewpoint of electromagnetics. The criterion for transition is when the magneto- or electro-quasi-static approximation is applicable. The transition frequency is approximately 100 kHz-10 MHz, although it highly depends on the source type and dimension (Hirata et al. 2013, Jin et al. 2012, Hand 2008). For exposure to lower frequencies ( $< 10$  MHz) where the quasi-static approximation is applicable, non-invasive brain stimulation is one of the emerging medical applications. Such approach may be used to avoid the significant inconsistency caused by the inter- and intra-subject variability (Rashed, Sakai, Gomez-Tames & Hirata 2019, Laakso

**Table 1.** Human head tissue conductivity ( $\sigma$ ) [S/m], relative permittivity ( $\epsilon$ ), and mass density ( $\rho$ ) [kg/m<sup>3</sup>] values at different radio-frequencies (Gabriel et al. 1996).

#	Tissue	$\rho$ (kg/m <sup>3</sup> )	900 MHz		1.8 GHz		3.0 GHz	
			$\sigma$	$\epsilon$	$\sigma$	$\epsilon$	$\sigma$	$\epsilon$
1	Blood	1050	1.54	61.36	2.04	59.37	3.05	57.35
2	Bone (Cancellous)	1178	0.34	20.79	0.59	19.34	1.01	17.94
3	Bone (Cortical)	1908	0.14	12.45	0.28	11.78	0.51	11.07
4	Brain (Grey Matter)	1145	0.94	52.73	1.39	50.08	2.22	48.05
5	Brain (White Matter)	1041	0.59	38.89	0.91	37.01	1.51	35.54
6	Cerebellum	1045	1.26	49.44	1.71	46.11	2.48	43.90
7	Cerebro Spinal Fluid	1007	2.41	68.64	2.92	67.20	4.01	65.39
8	Dura	1174	0.96	44.43	1.32	42.89	2.01	41.34
9	Fat	911	0.05	5.46	0.08	5.35	0.13	5.22
10	Mucous tissue	1102	0.84	46.08	1.23	43.85	1.95	42.11
11	Muscle	1090	0.94	55.03	1.34	53.55	2.14	52.06
12	Skin	1109	0.87	41.41	1.18	38.87	1.74	37.45
13	Vitreous Humor	1005	1.64	68.90	2.03	68.57	2.96	67.82

et al. 2015, López-Alonso et al. 2014). In a previous study, we succeeded in applying deep learning approaches to estimate the electrical conductivity based on MRI in low-frequency medical applications such as transcranial magnetic stimulation (TMS) (Rashed, Gomez-Tames & Hirata 2019b). The network architecture, which is known as CondNet, was able to provide high-quality estimation of a brain-induced electric field without tissue segmentation.

At frequencies higher than 10 MHz, personalized head models are used for radio-frequency hyperthermia (e.g. D’Andrea et al. 2007). In this regime, relative permittivity is also needed for full-wave analysis. In addition, the standardization of human protection from electromagnetic fields considers the inter-subject variability, and thus, the dosimetric evaluation of different human models has become essential (Liu et al. 2019, Susnjara et al. 2018, Li et al. 2018).

In the present study, we extend our previous work by considering a more demanding application such as radio-frequency exposure. Learning-based architecture is designed to estimate the dielectric properties, i.e., relative permittivity, in addition to the electrical conductivity, required for radio-frequency exposure using anatomical information from T1- and T2-weighted MRI. Moreover, it estimates the tissue mass density for the SAR calculations. A schematic demonstration of the current standard pipeline for computation of the head models for SAR calculations and the proposed approach is shown in Figure 1.

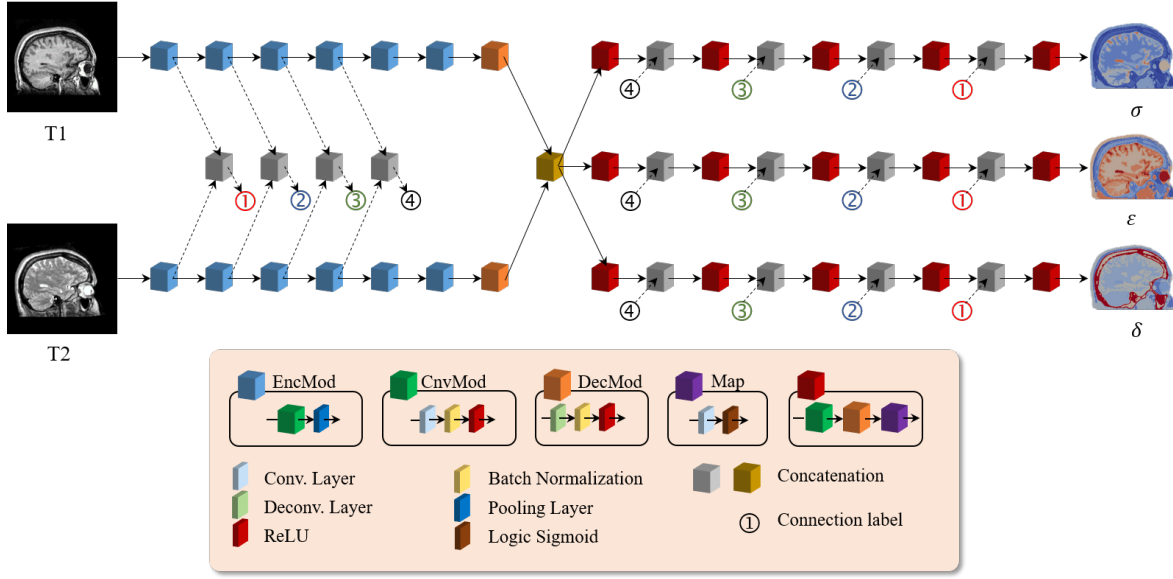


**Figure 2.** Design of the learning-based architecture and label key. The inputs are T1- and T2-weighted MRI, and the outputs are the conductivity ( $\sigma$ ), relative permittivity ( $\varepsilon$ ), and density ( $\rho$ ) maps. The dashed lines represent the skip connections, and the architecture feature size is listed in Table 2.

## 2. Materials and Methods

### 2.1. Anatomical dataset and preprocessing

In this study, a set of anatomical images corresponding to 18 subjects from the NAMIC: Brain Multimodality dataset<sup>‡</sup> are used. Each subject is assigned to T1- and T2-weighted MRI scans with a volume size of  $256^3$  voxels and resolution of  $1.0 \text{ mm}^3$ . Each subject is segmented into 13 different tissues using a semi-automatic method (Laakso et al. 2015), as listed in Table 1. The segmented models are assigned with uniform values of conductivity ( $\sigma$ ), relative permittivity ( $\varepsilon$ ), and density ( $\rho$ ), as listed in Table 1. The anatomical magnetic resonance images are normalized such that each subject has a zero mean and unit variance, followed by scaling in the range of  $[0, 1]$ . The conductivity, relative permittivity, and mass-density values are normalized using the following equations:

$$\tilde{\sigma}^r = \frac{(1 - \tau)\sigma^r}{\max_n(\sigma_n^r)}, \quad \tilde{\varepsilon}^r = \frac{(1 - \tau)\varepsilon^r}{\max_n(\varepsilon_n^r)}, \quad \tilde{\rho} = \frac{(1 - \tau)\rho}{\max_n(\rho_n)} \quad (1)$$








where  $\sigma_n^r$  and  $\varepsilon_n^r$  are the uniform conductivity and permittivity measured for tissue  $n$  at frequency  $r$ , respectively, and  $\tau$  is a parameter (here  $\tau = 0.1$ ).

### 2.2. Learning architecture

The objective of the learning architecture is to map the anatomical images ( $M^{T1}$  and  $M^{T2}$ ) to the dielectric properties and tissue density ( $\sigma^r$ ,  $\varepsilon^r$ , and  $\rho$ ) at frequency  $r$ .

<sup>‡</sup> <http://hdl.handle.net/1926/1687>

**Table 2.** Details of learning architecture shown in Figure 2.

Module	Layer	Output size	Label
Input <sub>u</sub> $u : 1 \rightarrow 2$		$256 \times 256$	
EncMod <sub>u,i</sub> $u : 1 \rightarrow 2$ $i : 1 \rightarrow 6$	Convolution BN & ReLU Pooling (Max)	$2^{(i+1)} \times [2^{(8-i)}]^2$ $2^{(i+1)} \times [2^{(8-i)}]^2$ $2^{(i+1)} \times [2^{(7-i)}]^2$	
DecMod <sub>u</sub> $u : 1 \rightarrow 2$	Deconvolution BN & ReLU	$64 \times 8 \times 8$ $64 \times 8 \times 8$	
Hub	Concatenation	$2 \times 64 \times 8 \times 8$	
CnvMod <sub>v,i</sub> $v : 1 \rightarrow V$ $i : 5 \rightarrow 1$	Convolution BN & ReLU	$2^{(i+2)} \times [2^{(8-i)}]^2$ $2^{(i+2)} \times [2^{(8-i)}]^2$	
DecMod <sub>v,i</sub> $v : 1 \rightarrow 3$ $i : 5 \rightarrow 1$	Deconvolution BN & ReLU	$2^{(i+1)} \times [2^{(9-i)}]^2$ $2^{(i+1)} \times [2^{(9-i)}]^2$	
Map <sub>v,i</sub> $v = 1 \rightarrow 3$ $i : 5 \rightarrow 1$	Convolution Sigmoid (Log)	$2^i \times [2^{(9-i)}]^2$ $\begin{cases} 2^i \times [2^{(9-i)}]^2 & i > 1 \\ [2^8]^2 & i = 1 \end{cases}$	
Concat <sub>v,i</sub> $v : 1 \rightarrow 3$ $i = 4 \rightarrow 1$	Concatenation	$3 \times 2^{(i+2)} \times [2^{(8-i)}]^2$	
Output <sub>v</sub> $v = 1 \rightarrow 3$		$256 \times 256$	

Therefore, the learning-architecture parameters are optimized to fit the training data by solving the following problem:

$$\min_{\Omega} f(M, \theta^r | \Psi), \quad (2)$$

where  $M = \{M^{T1}, M^{T2}\}$ ,  $\theta^r = \{\tilde{\sigma}^r, \tilde{\varepsilon}^r, \tilde{\rho}\}$ .  $f$  is the loss function, and  $\Psi$  represents the network parameters. The deep-learning architecture CondNet presented in Rashed, Gomez-Tames & Hirata (2019b) is extended to fit with the problem presented in this study. The architecture shown in Figure 2, which maps a dual input of T1- and T2-weighted MRI slices to a triple output, demonstrates the conductivity, relative permittivity, and tissue-density distributions. The main components of this learning architecture are the convolution and deconvolution operations, which concurrently operate to map the gray-scale values in MRI to the corresponding physical properties of the tissue. Encoders with several convolution operations are designed to independently learn the anatomical features, whereas decoders are developed to map these features to different tissue properties in a parallel manner. This strategy proves to be useful in improving the network learning (Rashed, Gomez-Tames & Hirata 2019a, Rashed, Gomez-Tames & Hirata 2019b). The size of the learned features at each network layer is listed in detail in Table 2. The estimated normalized physical properties are computed

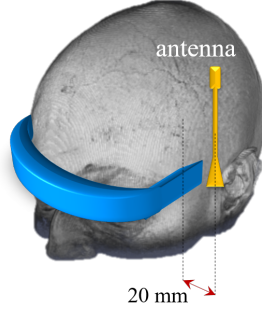


**Figure 3.** Demonstration of the simulated antenna position at the left temporal lobe.

as follows:

$$\{\sigma_k^r, \varepsilon_k^r, \rho_k\} = \text{CondNet}_r(M_k^{T1}, M_k^{T2}), \forall k \quad (3)$$

where  $M^{T1}$  and  $M^{T2}$  are the normalized T1- and T2-weighted MRI volumes, respectively, and subscript  $k$  denotes the slice number. The learning process is considered using slices extracted from the axial, sagittal, and coronal orientations. Therefore, the estimated physical properties are averaged as follows:

$$\begin{aligned} \sigma_*^r &= \frac{1}{3}(\sigma_a^r + \sigma_s^r + \sigma_c^r), \\ \varepsilon_*^r &= \frac{1}{3}(\varepsilon_a^r + \varepsilon_s^r + \varepsilon_c^r), \\ \rho_* &= \frac{1}{3}(\rho_a + \rho_s + \rho_c), \end{aligned} \quad (4)$$

where  $\sigma_a$ ,  $\sigma_s$ , and  $\sigma_c$  are the conductivity volume maps estimated using the axial, sagittal, and coronal slices, respectively. In the same manner,  $\varepsilon_*$  and  $\rho_*$  are computed. The learning-based conductivity, relative permittivity, and tissue-density maps are computed by re-scaling using the following equations:

$$\hat{\sigma}^r = \frac{\max_n(\sigma_n^r)}{1 - \tau} \sigma_*^r, \quad \hat{\varepsilon}^r = \frac{\max_n(\varepsilon_n^r)}{1 - \tau} \varepsilon_*^r, \quad \hat{\rho} = \frac{\max_n(\rho_n)}{1 - \tau} \rho_*. \quad (5)$$

### 2.3. Radio-frequency exposure from a dipole antenna

We consider a scenario where the head is exposed to a dipole antenna at radio frequency. This setup is a canonical one considering the exposure from wireless communication devices, e.g., using mobile phones. The radiation source is a half-wavelength dipole antenna located 20 mm from the scalp close to the temporal lobe, as shown in Figure 3, with a total emitted power of 1 W. The finite-difference time-domain (FDTD) method (Taflov & Hagness 2005) is adopted to solve the electromagnetic problem. The dipole antenna is orientated parallel to the longitudinal axis of the body. The antenna lengths are 15.7, 7.9, and 2.4 cm at 0.9, 1.8, and 3.0 GHz, respectively. A 10-layer convolutional

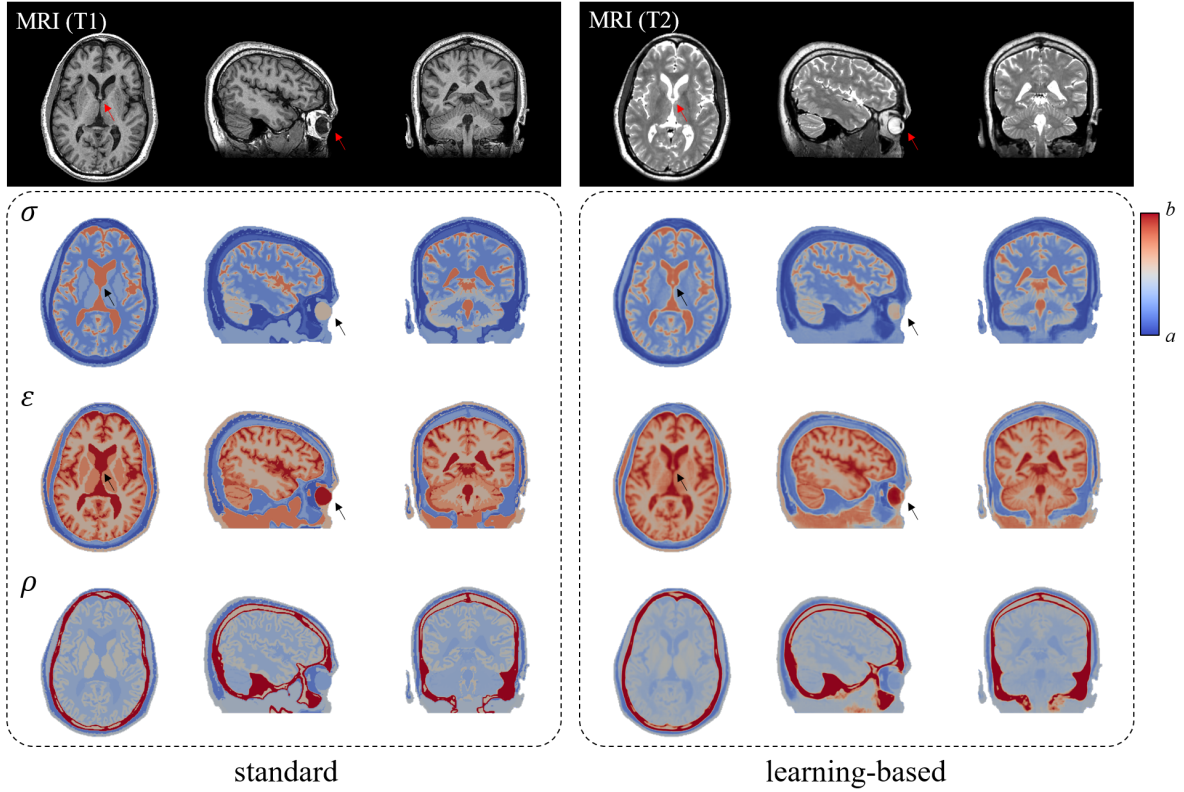


**Figure 4.** Sample result of a subject (case01039). Anatomical images (top) and corresponding physical properties (bottom) computed using the standard and learning-based approaches at 900 MHz. The color scale is defined as  $[a, b] = [0.0, 3.0]$ ,  $[0.0, 70.0]$ , and  $[800, 1500]$  for  $\sigma$ ,  $\varepsilon$ , and  $\rho$ , respectively. The arrows indicate the regions where the learning-based maps exhibit a higher consistency with the anatomical images.

perfectly matched layer (CPML) (Roden & Gedney 2000) is adopted to truncate the simulation domain. The total simulation domain contains  $290^3$  voxels. SAR is obtained by the following:

$$SAR = \frac{\sigma(t)}{\rho(t)} |E(t)|^2, \quad (6)$$

where  $|E(t)|$  is the rms value of the calculated electric field at  $t(x, y, z)$  inside the head model.

#### 2.4. Metrics for evaluation

For quantitative evaluation of the SAR distribution, we compute the absolute error using the following equation:

$$E = \frac{\sum_{i \in \Omega} |SAR(i) - \overline{SAR}(i)|}{\sum_{i \in \Omega} 1} \quad (7)$$

where  $SAR$  and  $\overline{SAR}$  are the SAR maps computed using the standard and learning-based approaches, respectively, and  $\Omega$  is the subject head volume. The error values



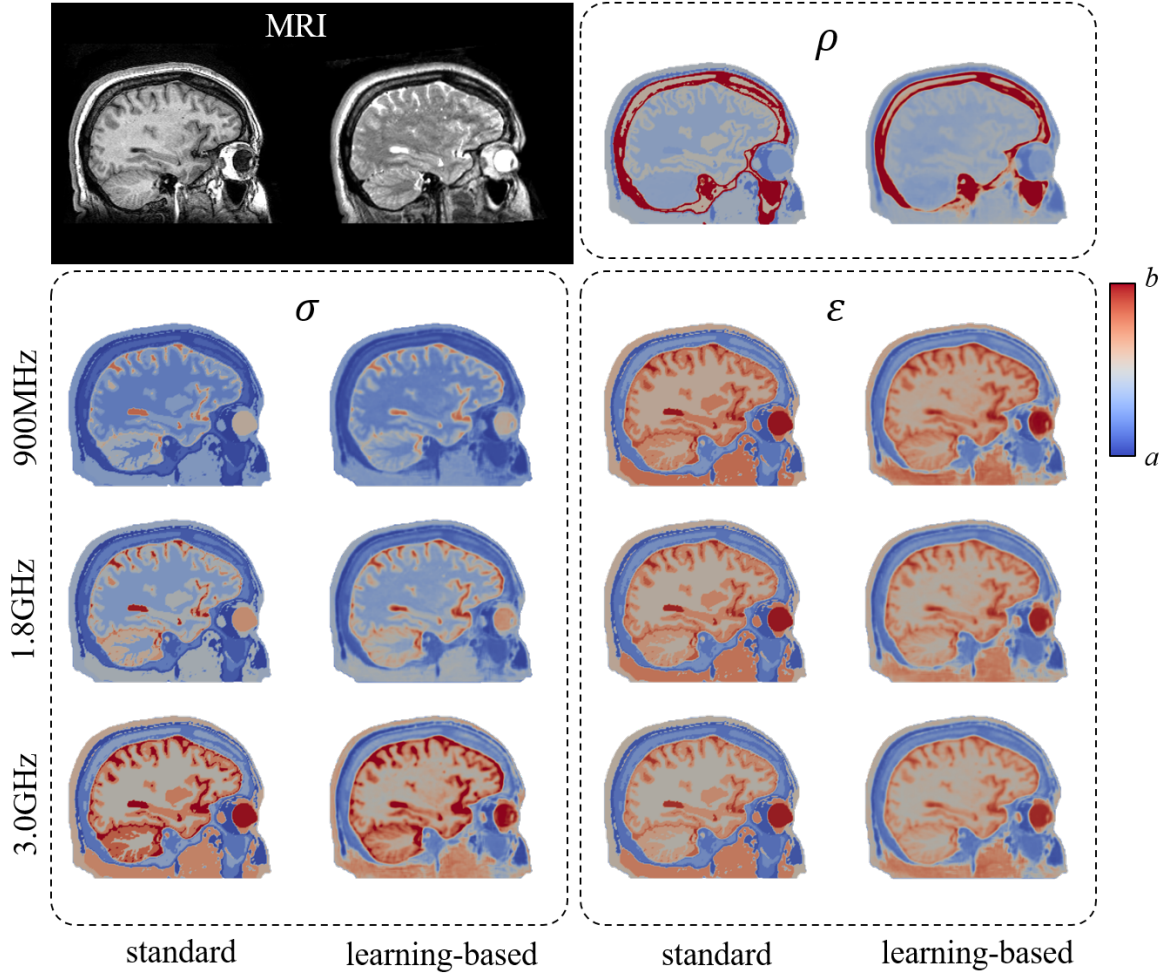


**Figure 5.** Physical properties computed using the standard and proposed (learning-based) approaches at different radio frequencies. The top left shows the anatomical images. The top right shows the density maps ( $\text{kg}/\text{m}^3$ ). The bottom left and right represent the conductivity ( $\text{S}/\text{m}$ ) and relative permittivity maps at 900 MHz, 1.8 GHz, and 3.0 GHz frequencies, respectively. The color scale is defined as  $[a, b] = [0.0, 3.0]$ ,  $[0.0, 70.0]$ , and  $[800, 1500]$  for  $\sigma$ ,  $\varepsilon$ , and  $\rho$ , respectively.

computed at different frequencies are listed in Table 3. Moreover, the SAR value, which is averaged over 10 g of tissue in a cubic shape ( $\text{SAR}^{10g}$ ) excluding the air voxels, of the different subjects is calculated, and the peak spatial averaged SAR ( $ps\text{SAR}$ ) values are listed in Table 4. We also compute the relative error as

$$E_{\max} = \frac{|ps\text{SAR} - \overline{ps\text{SAR}}|}{ps\text{SAR}}, \quad (8)$$

### 3. Results

#### 3.1. Conductivity, permittivity, and density estimation

The proposed architecture, which is an extension of CondNet, is trained to estimate the  $\sigma$ ,  $\varepsilon$ , and  $\rho$  maps using normalized T1- and T2-weighted MRI. Ten arbitrarily selected subjects are employed for optimization of the network parameters through training that uses the cross-validation loss function. The number of subjects required for the training was determined in our previous work, and we have determined that 10 to 15 subjects are sufficient for reasonable training (Rashed, Gomez-Tames & Hirata 2019a). In the training phase, two-dimensional MRI slices are mapped to the corresponding uniform physical properties computed using the standard approach shown in Figure 1. The slices are extracted from different orientations (i.e., axial, sagittal, and coronal) in which each slice is used to train the individual network. Training is conducted through 50 epochs with a batch size of four slices and using the ADAM optimizer (Kingma & Ba 2014). The remaining eight subjects are tapped for evaluation of the training-based estimation. The network outputs from different slicing directions are averaged to generate the estimated  $\sigma$ ,  $\varepsilon$ , and  $\rho$  maps. The learning-based architecture is implemented using four 3.60-GHz Intel (R) Xeon CPU workstation with a 128-GB memory and three NVIDIA GeForce GTX 1080 GPUs. The computation is performed using the GPUs, and a single training phase is completed in approximately 19.2 min. Testing of a single subject requires approximately 12.4 s. An example of the estimated physical properties at a frequency of 900 MHz is shown in Figure 4. From these results, we can clearly see that the learning-based  $\sigma$ ,  $\varepsilon$ , and  $\rho$  maps are highly consistent with those computed using the standard pipeline. However, the learning-based maps show a smoother pattern (see transition within region borders). This result can be attributed to the ability of the learning architecture to estimate the water contents using the gray-scale value of anatomical images.

The training is repeated at frequencies of 1.8 and 3.0 GHz, and an example of the estimated  $\sigma$ ,  $\varepsilon$ , and  $\rho$  maps is shown in Figure 5. From these data, we can observe that the standard method provides a consistent value within the same anatomical regions with high-contrast edges. However, the learning-based values have more realistic (smooth transit) patterns. Moreover, we can observe some regions where the learning-based maps demonstrate higher consistency with the anatomical regions, as shown by the arrows in Figure 4. To highlight how accurate are the estimated learning-based physical-property maps, we compute the mean and standard deviation of each head tissue by testing eight subjects. The values that represent the distributions of  $\hat{\sigma}$ ,  $\hat{\varepsilon}$ , and  $\hat{\rho}$  are shown in Figure 6, which shows that the head tissues presented in high contrast (e.g., white matter, gray matter, and bone) in the anatomical images are estimated with higher accuracy than the low-contrast tissues (e.g., dura, blood, and mucous tissues).

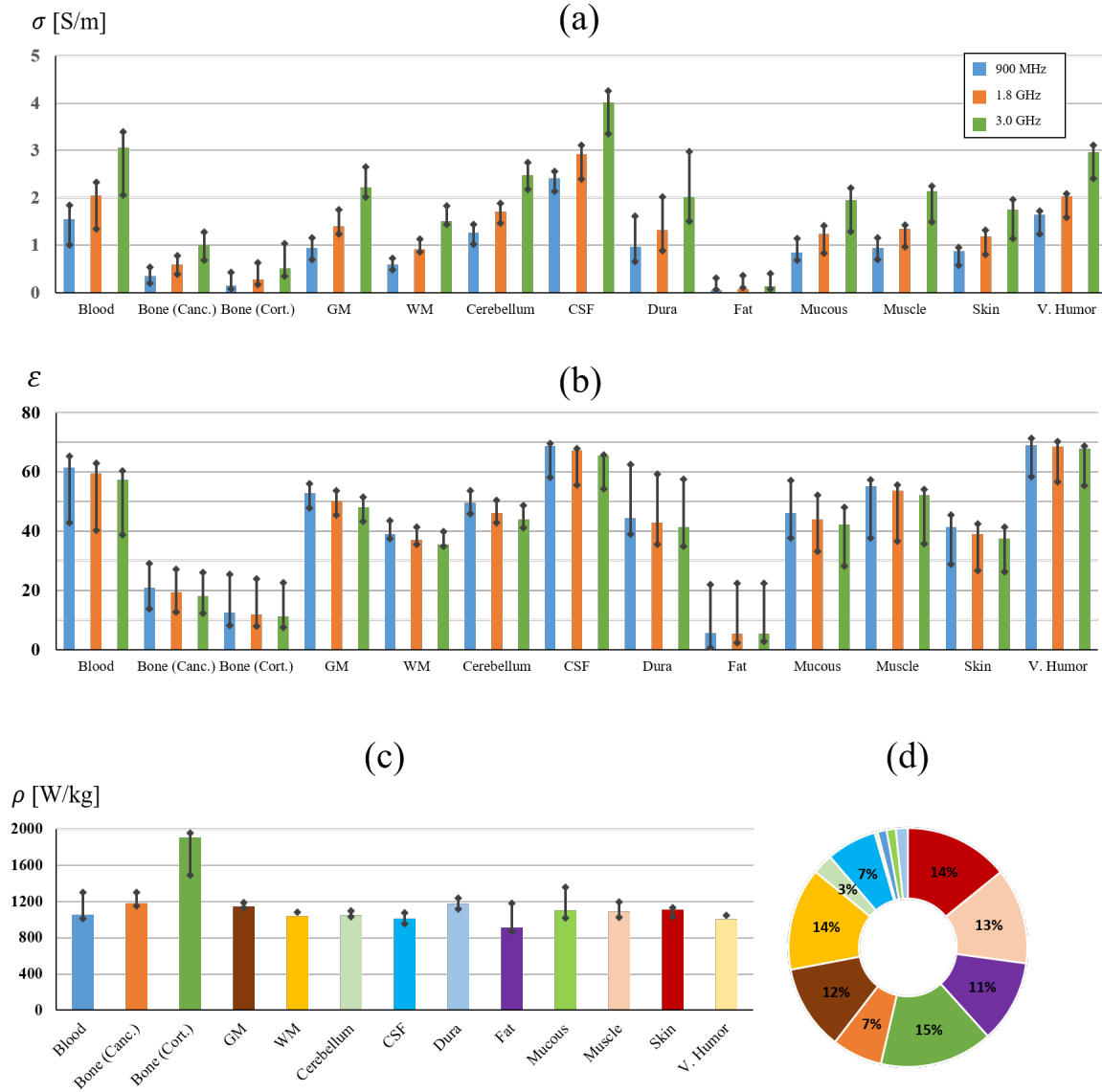


**Figure 6.** Standard and learning-based dielectric properties and tissue-density values of the different head tissues in eight subjects computed at different frequencies. (a) Electrical conductivity, (b) relative permittivity, and (c) tissue density. The color bars represent the constant standard values (Table 1), and the black lines indicate the learning-based value range (mean $\pm$ std). The doughnut chart in (d) shows the average volume ratio of each tissue. Tissue annotation in the standard approach is used as the golden-truth segmentation.

### 3.2. SAR evaluation

To evaluate the proposed method for safety assessments, two studies are conducted to compute the SAR distributions in the head using the standard physical properties assigned to the segmented models and the learning-based values without segmentation. The radio-frequency exposure from the antenna located close to the left of the temporal lobe, as shown in Figure 3, is considered. The computed results are shown in Figure 7, which indicate that consistent results can be achieved in the axial, sagittal, and coronal directions. The major difference is that the SAR distributions computed using the learning-based approach exhibit a texture with smooth transitions. Another example that demonstrates the SAR distribution at different frequencies is shown in Figure 8. Again, a consistent SAR distribution is observed, as shown by the magnified regions in Figure 9. A single coronal slice of the SAR distribution at 900 MHz in all subjects is extracted and shown in Figure 10. The same behavior with different levels of consistency is observed in all eight tested subjects, which demonstrates the validity of the learning-based approach.

From the list in Table 3, we can observe a small change in the SAR values in all subjects with maximum error  $E = 0.071$ , whereas the maximum average error in all subjects is 0.051. In addition, the quantitative evaluation of the *ps*SAR values indicates a relatively small change in the different subjects with a maximum error of approximately 15%. The average maximum 10-g SAR in the eight subjects reflects high matching with errors of 1.95%, 3.37%, and 3.76% at 900 MHz, 1.8 GHz, and 3.0 GHz, respectively.

## 4. Discussion

In recent studies, deep-learning approaches have been applied to directly estimate the induced physical quantities from a given source (Yokota et al. 2019, Meliadoro et al. 2019). Meliadoro et al. (2019) proposed a SAR-estimation method using B1<sup>+</sup> maps and demonstrated the results using the prostate-imaging application. The results indicated good matching in the spatial-average SAR estimation with reduction in the computation time. However, direct estimation of the averaged SAR from CNN requires careful consideration of several parameters (such as the source position, orientation, and frequency). Yokota et al. (2019) estimated the induced electric field from a coil located at different places. Again, the source was fixed. Thus, these approaches are powerful only when the source parameters are fixed or its flexibility is small because the variations of all these potential variables require a huge amount of training dataset that demonstrate several potential challenges.

The use of personalized electromagnetic exposure requires enhancement of the current standard approach. However, accurate calculations require a high-quality annotation of the different tissue compositions in the biological object under study. This process is considered to be a challenging task considering the large variability in the electrical field in a human body and consequently in the variability of the resulting

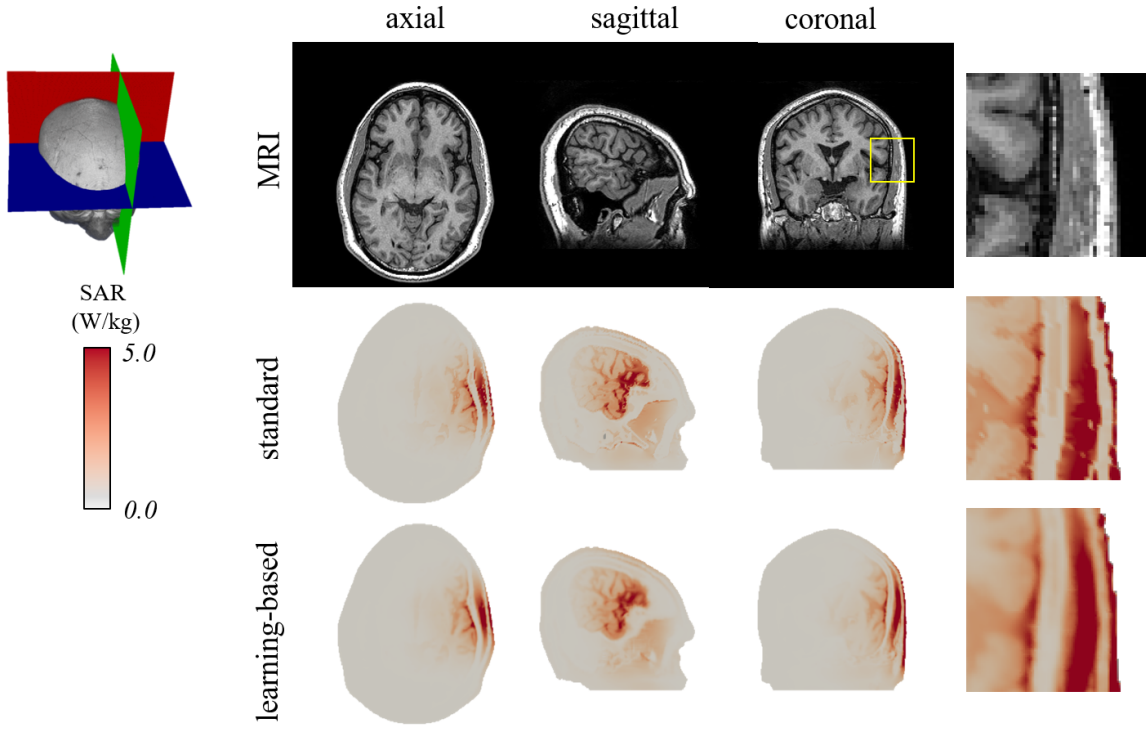


**Figure 7.** SAR maps of one subject at different orientations computed using the standard and learning-based approaches with the corresponding anatomical image. The regions labeled by the yellow square are magnified and shown at the rightmost column. At the left side, the axial, sagittal, and coronal-slice positions are shown in blue, green, and red colors, respectively.

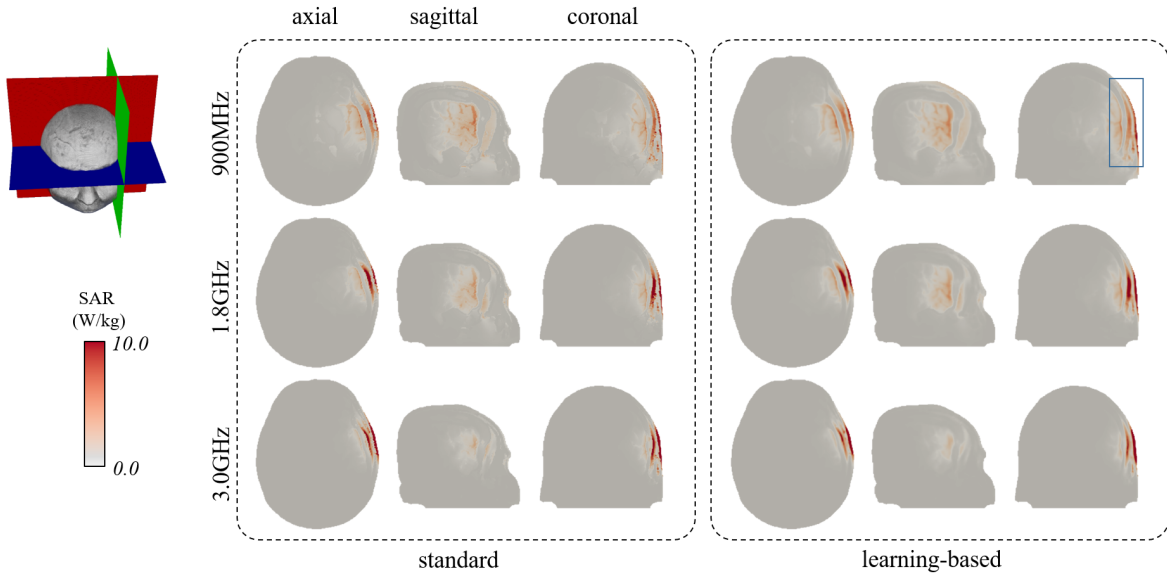


**Figure 8.** SAR distribution at different orientations computed using the uniform and learning-based physical properties at different frequencies. The slice positions are shown at the left side. A magnification of the region labeled with the blue rectangle is shown in Figure 9 for different exposure setups.

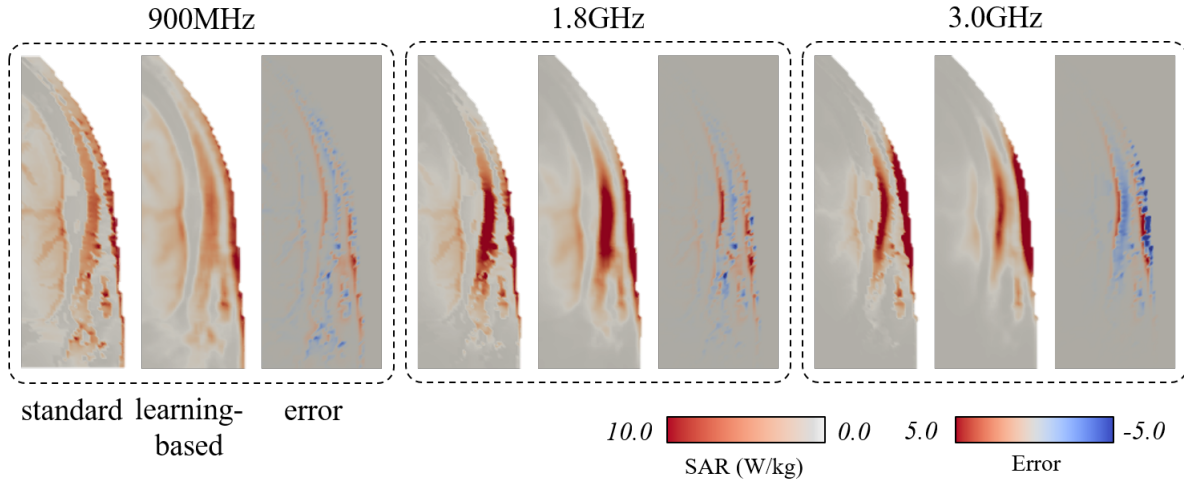


**Figure 9.** Magnified region of the SAR distribution in the coronal direction of the subject shown in Figure 8 computed using the different approaches and at different frequencies with their associated error.

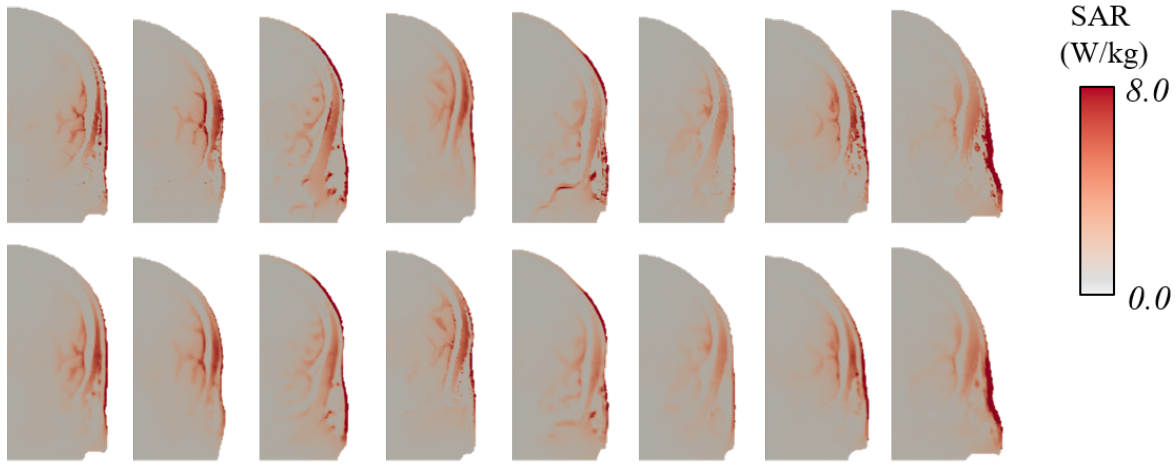


**Figure 10.** Truncated coronal slices of the computed SAR maps of the eight subjects computed using the standard (top) and learning-based (bottom) approaches.

SAR distributions. This work presents a novel framework for automatic estimation of the dielectric properties and tissue density of all head tissues directly from MRI. The proposed method is easy to use and does not require highly sophisticated imaging protocols. The learning-based dielectric properties can be estimated with high accuracy without segmentation. Moreover, the tissue mass density is estimated using a single-step network validation. The learning-based estimated values are used to assess the SAR distribution, and the results provide good matching with those computed using the standard approach. Nevertheless, the learning-based approach provides a smoother distribution with a relatively small average difference. For further validation as well as

**Table 3.** Absolute error ( $E$ ) of SAR values for different subjects at different frequencies ( $\times 10^{-2}$ ).

#	Subject	900 MHz	1.8 GHz	3.0 GHz
1	case01017	4.536	3.200	2.441
2	case01019	4.878	3.033	2.352
3	case01025	7.114	4.751	3.564
4	case01028	4.278	2.628	1.949
5	case01034	5.909	3.473	1.909
6	case01039	4.443	3.357	2.878
7	case01042	5.260	3.701	3.459
8	case01045	4.075	2.944	1.686
average		5.062	3.386	2.529

**Table 4.**  $psSAR$  computed from SAR maps generated using standard (S) and learning-based (L) approaches with relative error ( $E_{\max}$ ) for different subjects at different frequencies.

#	Subject	900 MHz			1.8 GHz			3.0 GHz		
		S	L	E	S	L	E	S	L	E
1	case01017	2.780	2.966	6.69%	3.998	4.156	3.95%	3.901	3.320	14.90%
2	case01019	3.363	3.280	2.45%	3.723	3.737	0.39%	3.851	3.983	3.42%
3	case01025	2.817	2.966	5.32%	3.488	3.828	9.75%	4.245	4.194	1.20%
4	case01028	3.060	3.172	3.64%	3.228	3.291	1.93%	3.625	3.661	0.99%
5	case01034	3.362	3.289	2.16%	3.607	3.665	1.62%	3.148	3.326	5.63%
6	case01039	2.488	2.690	8.10%	3.607	3.978	10.29%	3.587	3.146	12.28%
7	case01042	2.634	2.755	4.57%	3.544	3.839	8.33%	3.015	2.622	13.02%
8	case01045	3.632	3.488	3.95%	5.369	5.101	5.00%	3.110	3.161	1.62%
average		3.017	3.076	1.95%	3.821	3.949	3.37%	3.560	3.427	3.76%

for practical application, the peak value of 10-g average SAR is computed. The results indicate that the learning-based method using CondNet has a high-consistency value with the standard method. It achieves an average relative difference of less than 3.77%.

The generation of a personalized head model is a more realistic approach for human safety application at radio frequency because a substantial number of computational data are needed for variability analysis, namely, different exposure scenarios with different sources, distances, and orientation, because the antenna-human coupling is significant, especially when their separation is in the near-field regime. In the low-frequency dosimetry for medical application, more than 200,000 cases are considered to learn the different source positions (Yokota et al. 2019). Developing a learning-based method that can consider a wide range of exposure scenarios with all potential varieties of experimental setup remains a challenge. However, the time can be significantly reduced by avoiding extensive segmentation, especially when the number of tissues is large and with some tissues hardly being observed in the anatomical image. This work is a step forward toward a fully automatic simulation using deep learning.



## 5. Conclusion

Learning-based estimation of the physical properties of human head models has been presented. Once the network is trained, the estimated non-uniform values of conductivity, permittivity, and mass-density values can be automatically generated in a single shot. The learning-based dielectric properties as well as the tissue density demonstrate high-consistency patterns with those generated using the standard pipeline that employs time-consuming segmentation. The proposed approach demonstrates several advantages. It provides a more robust approach with better representation of the corresponding anatomy. The heterogeneous physical properties exhibit a smoother pattern, resulting in a smoother SAR distribution. The computed results for a dipole antenna indicate that the SAR distribution of the proposed approach is highly consistent with that of the standard approach.

## Acknowledgment

This work was supported in part by JSPS KAKENHI Grant Number17H00869.

## Supplementary data

A short video that shows a 3D view of the SAR distribution in the head of a single subject using the standard (left) and learning-based (right) approaches is available in this link [https://youtu.be/3FU9NsKD\\_K0](https://youtu.be/3FU9NsKD_K0).

## References

- Bengio, Y., Courville, A. & Vincent, P. (2013). Representation learning: A review and new perspectives, *IEEE Trans. Pattern Anal. Mach. Intell.* **35**(8): 1798–1828.
- Chauhan, M., Indahlastari, A., Kasinadhuni, A. K., Schar, M., Mareci, T. H. & Sadleir, R. J. (2018). Low-frequency conductivity tensor imaging of the human head in vivo using DT-MREIT: First study, *IEEE Trans. Med. Imaging* **37**(4): 966–976.
- Christ, A., Chavannes, N., Nikoloski, N., Gerber, H.-U., Poković, K. & Kuster, N. (2005). A numerical and experimental comparison of human head phantoms for compliance testing of mobile telephone equipment, *Bioelectromagnetics* **26**(2): 125–137.
- D’Andrea, J. A., Zirias, J. M. & Adair, E. R. (2007). Radio frequency electromagnetic fields: mild hyperthermia and safety standards, in H. S. Sharma (ed.), *Neurobiology of Hyperthermia*, Vol. 162 of *Progress in Brain Research*, Elsevier, pp. 107–135.
- Dimbylow, P. J. (1997). FDTD calculations of the whole-body averaged SAR in an anatomically realistic voxel model of the human body from 1 MHz to 1 GHz, *Phys. Med. Biol.* **42**(3): 479–490.
- Elsaid, N. M. H., Nachman, A. I., Ma, W., DeMonte, T. P. & Joy, M. L. G. (2017). The impact of anisotropy on the accuracy of conductivity imaging: A quantitative validation study, *IEEE Trans. Med. Imaging* **36**(2): 507–517.
- Gabriel, S., Lau, R. W. & Gabriel, C. (1996). The dielectric properties of biological tissues: II. measurements in the frequency range 10 Hz to 20 GHz, *Phys. Med. Biol.* **41**(11): 2251–2269.



- Gurler, N. & Ider, Y. Z. (2017). Gradient-based electrical conductivity imaging using MR phase, *Magn. Reson. Med.* **77**(1): 137–150.
- Hampe, N., Herrmann, M., Amthor, T., Findekle, C., Doneva, M. & Katscher, U. (2019). Dictionary-based electric properties tomography, *Magn. Reson. Med.* **81**(1): 342–349.
- Hand, J. W. (2008). Modelling the interaction of electromagnetic fields (10 MHz–10 GHz) with the human body: methods and applications, *Phys. Med. Biol.* **53**(16): R243–R286.
- Hirata, A., Ito, F. & Laakso, I. (2013). Confirmation of quasi-static approximation in SAR evaluation for a wireless power transfer system, *Phys. Med. Biol.* **58**(17): N241–N249.
- Jin, J., Liu, F., Weber, E. & Crozier, S. (2012). Improving SAR estimations in MRI using subject-specific models, *Phys. Med. Biol.* **57**(24): 8153–8171.
- Kingma, D. P. & Ba, J. (2014). Adam: A method for stochastic optimization, *arXiv:1412.6980*.
- Kwon, O. I., Jeong, W. C., Sajib, S. Z. K., Kim, H. J. & Woo, E. J. (2014). Anisotropic conductivity tensor imaging in MREIT using directional diffusion rate of water molecules, *Phys. Med. Biol.* **59**(12): 2955–2974.
- Kwon, O. I., Sajib, S. Z. K., Sersa, I., Oh, T. I., Jeong, W. C., Kim, H. J. et al. (2016). Current density imaging during transcranial direct current stimulation using DT-MRI and MREIT: Algorithm development and numerical simulations, *IEEE Trans. Biomed. Eng.* **63**(1): 168–175.
- Laakso, I., Tanaka, S., Koyama, S., Santis, V. D. & Hirata, A. (2015). Inter-subject variability in electric fields of motor cortical tDCS, *Brain Stimul.* **8**(5): 906–913.
- Lee, A., Hong, S., Kwon, J. & Choi, H. (2015). SAR comparison of SAM phantom and anatomical head models for a typical bar-type phone model, *IEEE Trans. Electromagn. C.* **57**(5): 1281–1284.
- Li, C., Sun, X. & Wu, T. (2018). Dosimetric Comparison Using the Human Models Reconstructed by Precise Segmentation, Tissue Simplification and Template Based Registration, *12th European Conference on Antennas and Propagation (EuCAP 2018)*, Institution of Engineering and Technology, p. 135 (3 pp.).
- Liao, Y., Lechea, N., Magill, A. W., Worthoff, W. A., Gras, V. & Shah, N. J. (2019). Correlation of quantitative conductivity mapping and total tissue sodium concentration at 3T/4T, *Magn. Reson. Med.* **82**(4): 1518–1526.
- Liu, J., Wang, Y., Katscher, U. & He, B. (2017). Electrical properties tomography based on  $B_1$  maps in MRI: Principles, applications, and challenges, *IEEE Trans. Biomed. Eng.* **64**(11): 2515–2530.
- Liu, W., Wang, H., Zhang, P., Li, C., Sun, J., Chen, Z., Xing, S., Liang, P. & Wu, T. (2019). Statistical Evaluation of Radiofrequency Exposure during Magnetic Resonant Imaging: Application of Whole-Body Individual Human Model and Body Motion in the Coil, *International Journal of Environmental Research and Public Health* **16**(6): 1069.
- López-Alonso, V., Cheeran, B., Rio-Rodriguez, D. & del Olmo, M. F. (2014). Inter-individual variability in response to non-invasive brain stimulation paradigms, *Brain Stimul.* **7**(3): 372–380.
- Meliadò, E., Raaijmakers, A., Sbrizzi, A., Steensma, B., Maspero, M., Savenije, M., Luijten, P. & van den Berg, C. (2019). A deep learning method for image-based subject-specific local SAR assessment, *Magn. Reson. Med.* **83**(2): 695–711.
- Michel, E., Hernandez, D. & Lee, S. Y. (2017). Electrical conductivity and permittivity maps of brain tissues derived from water content based on T1-weighted acquisition, *Magn. Reson. Med.* **77**(3): 1094–1103.
- Nagaoka, T., Watanabe, S., Sakurai, K., Kunieda, E., Watanabe, S., Taki, M. & Yamanaka, Y. (2004). Development of realistic high-resolution whole-body voxel models of Japanese adult males and females of average height and weight, and application of models to radio-frequency electromagnetic-field dosimetry, *Phys. Med. Biol.* **49**(1): 1–15.
- Rashed, E. A., Gomez-Tames, J. & Hirata, A. (2019a). Development of accurate human head models for personalized electromagnetic dosimetry using deep learning, *NeuroImage* **202**: 116132.
- Rashed, E. A., Gomez-Tames, J. & Hirata, A. (2019b). Non-uniform conductivity estimation for personalized brain stimulation using deep learning, *arXiv* **1910.02420**.
- Rashed, E. A., Sakai, T., Gomez-Tames, J. & Hirata, A. (2019). Brain AI: deep learning for brain

- stimulation, *IEEE Pulse* **10**(4): 3–5.
- Roden, J. A. & Gedney, S. D. (2000). Convolution PML (CPML): An efficient FDTD implementation of the CFS–PML for arbitrary media, *Microw. Opt. Techn. Lett.* **27**(5): 334–339.
- Ropella, K. M. & Noll, D. C. (2017). A regularized, model-based approach to phase-based conductivity mapping using MRI, *Magn. Reson. Med.* **78**(5): 2011–2021.
- Serralles, J. E., Giannakopoulos, I., Zhang, B., Ianniello, C., Cloos, M. A., Polimeridis, A. G. et al. (2019). Noninvasive estimation of electrical properties from magnetic resonance measurements via global Maxwell tomography and match regularization, *IEEE Trans. Biomed. Eng.* . (in press).
- Susnjara, A., Cvetkovic, M., Poljak, D. & Dodig, H. (2018). Stochastic sensitivity analysis for dosimetry of head tissues for the three compartment head model, *2018 3rd International Conference on Smart and Sustainable Technologies (SpliTech)*, pp. 1–7.
- Taflove, A. & Hagness, S. C. (2005). *Computational electrodynamics: the finite-difference time-domain method*, Artech house.
- Tuch, D. S., Wedeen, V. J., Dale, A. M., George, J. S. & Belliveau, J. W. (2001). Conductivity tensor mapping of the human brain using diffusion tensor MRI, *Proc. Nat. Acad. Sci.* **98**(20): 11697–11701.
- Yokota, T., Maki, T., Nagata, T., Murakami, T., Ugawa, Y., Laakso, I., Hirata, A. & Hontani, H. (2019). Real-time estimation of electric fields induced by transcranial magnetic stimulation with deep neural networks, *Brain Stimul.* . (in press).